ADVANCED MATERIALS
www.advmat.de

Residue-Free Fabrication of 2D Materials Using van der Waals Interactions

*Minyoung Lee, Changho Kim, Soon-Yong Kwon, Kayoung Lee, Giyoon Kwak, Hyunseob Lim, and Jae Hun Seol**

2D materials have garnered considerable attention due to their distinctive properties, prompting diverse applications across various domains. Beyond their inherent qualities, the significance of 2D materials extends into the fabrication processes that can lead to the degradation of intrinsic performance through undesirable mechanical defects and surface contaminations. Herein, a novel fabrication technique to achieve residue-free 2D materials using van der Waals (vdW) interactions, primarily employing molybdenum disulfide (MoS_2) is proposed. Optical and electrical characterizations confirm the absence of residues, mechanical defects, oxidation, and strain, along with a prominent field-effect mobility of up to 60 $cm^2\ V^{-1}\ s^{-1}$ and an on/off ratio of $\approx 10^8$. Furthermore, the utilization of residue-free material as a stamp enables various manipulations of flakes transferred on substrates in advance, including pick-up and release, stacking, exfoliation, wiping-out, flipping, and smoothing-out processes. Additionally, the manipulation techniques also facilitate the fabrication of vdW heterostructures with precise positioning and the desired stacking order. In this regard, the feasibility of applying this method to hexagonal boron nitride and graphite is demonstrated. It is expected that this method will offer a versatile and effective approach to enhancing the qualities of 2D material-based electronic and optoelectronic devices.

1. Introduction

Beyond the distinctive intrinsic properties of 2D materials lies a crucial aspect in fabrication processes that could potentially degrade their intrinsic performance through undesirable mechanical damage and surface contamination.[1–5] Polymer materials like poly(methyl methacrylate) (PMMA) play vital roles in wet and dry transfers, as well as in the precise patterning of 2D materials and device components. However, removing these polymers during fabrication poses challenges, as a significant amount of polymer and chemical residues often remain on the surface of 2D materials even after harsh chemical treatments.[6,7] Hence, it is essential to develop an effective technique for preserving the exceptional properties of 2D materials, including large-scale fabrication, manipulation, and their integration into specific devices.

In recent times, a variety of advanced methodologies have already been demonstrated to achieve residue-free 2D materials, considering factors such as quality, size, yield, and implemental convenience. Given that PMMA serves the essential roles of providing support and protection for delicate 2D materials, strategies for enhancing high-quality 2D material production involve exploring alternatives such as poly(propylene carbonate), metal films, and even unconventional choices such as ice.[8–10] Simultaneously, endeavors to eliminate residues offer sophisticated techniques such as using atomic force microscopy (AFM), resulting in a remarkable reduction in impurities.[1] However, exposure to heterogeneous substances, coupled with factors like temperature and pressure changes, could still compromise the versatility and quality of 2D materials. Remarkably, van der Waals (vdW) interaction emerges as a

M. Lee, C. Kim, J. H. Seol
School of Mechanical and Robotics Engineering
Gwangju Institute of Science and Technology (GIST)
123 Cheomdangwagi-ro, Buk-gu, Gwangju 61005, Republic of Korea
E-mail: jhseol@gist.ac.kr

S.-Y. Kwon
Department of Materials Science and Engineering
Graduate School of Semiconductor Materials and Devices Engineering
Ulsan National Institute of Science and Technology (UNIST)
50 UNIST-gil, Eonyang-eup, Ulju-gun, Ulsan 44919, Republic of Korea

K. Lee
School of Electrical Engineering
Korea Advanced Institute of Science and Technology (KAIST)
291, Daehak-ro, Yuseong-gu, Daejeon 34141, Republic of Korea

G. Kwak, H. Lim
Department of Chemistry
Gwangju Institute of Science and Technology (GIST)
123 Cheomdangwagi-ro, Buk-gu, Gwangju 61005, Republic of Korea

The ORCID identification number(s) for the author(s) of this article can be found under https://doi.org/10.1002/adma.202418669

DOI: 10.1002/adma.202418669

promising polymer-free approach, especially for assembling vdW heterostructures.[11] Nonetheless, there is still a lack of research on various materials, and to the best of our knowledge, no instance has been reported where a handling material with vdW interactions was identical to the target material. Furthermore, intricate processes and costly equipment underscore the widening of the usability of the technique involving vdW interaction.

In addition to the transfer of 2D materials, the manipulation of these materials emerges as a critical aspect in fabricating 2D materials-based devices, requiring precise control over their shape, thickness, and positioning. Furthermore, achieving such manipulation without any polymer residue in vdW heterostructures has been substantially needed, considering the enhancement of electrical and optical performance of 2D material-based devices.[12,13] Conventionally, poly(dimethylsiloxane) or viscoelastic polymers have been applied to build up vdW heterostructures. However, the inevitably generated residues on the surface and interfaces hinder the achievement of flawless heterojunctions.[14,15] To address this issue, dry pick-and-flip assembly methods have been developed to ensure atomically clean surfaces and interfaces.[16,17] Additionally, a micro-dome polymer structure facilitates 3D manipulation of hexagonal boron nitride (h-BN), thereby expanding the possibilities for assembling a complex 3D heterostructure.[18] Nevertheless, further improvements are required in the aspect of using polymers, as sample contamination can result from direct contact with the polymers and potentially from residues left on the substrate during rinsing or wetting processes. In contrast, flexible silicon nitride coated with thin metal layers can be used as a stamp to create polymer-free vdW heterostructures with exceptionally clean interfaces, allowing for processing in high-temperature and ultra-high vacuum environments.[19] Although this method is well-suited for stacking 2D materials to construct heterostructures, it must be accompanied by precise tuning of the adhesion properties by adjusting the Au thickness (sub-1 nm) is essential to achieve the desired heterostructure configuration. From this perspective, our methods effectively address this issue by transferring and manipulating a 2D target flake with a residue-free stamp (RFS), which is the same type of material and operates based on vdW interaction between the target material and the RFS.

In this work, molybdenum disulfide (MoS_2) was mostly used for demonstrating our techniques, considering its high interfacial adhesive energy.[20] Residue-free flakes of MoS_2 are obtained through selective transfer processes: stamping (SM) and tearing methods (TM). Comprehensive investigations employing high-resolution transmission electron microscopy (HR-TEM), AFM, X-ray photoelectron spectroscopy (XPS), and Raman spectroscopy consistently manifested the absence of contaminations, damage, and strain on the samples. Exceptional electrical performance of the residue-free MoS_2 field-effect transistors (FETs) was observed through measurements of FET mobility and on/off ratio in different geometries. Furthermore, the RFS facilitates various manipulation techniques, including pick-up, release, stacking, exfoliation, wiping-out, flipping, and smoothing-out. Using this approach, h-BN/MoS_2/multilayer graphene (MLG) heterostructure was successfully assembled using the same material-based RFSs, which highlights its remarkable accessibility and versatility. We envision that this proposed method can be readily applied to the fabrication of high-quality 2D material-based devices, thereby broadening the scope of applications involving 2D materials.

2. Results and Discussion

2.1. Residue-Free Fabrication Procedure

Our fabrication processes make a significant advancement in achieving residue-free 2D materials, thoroughly avoiding exposure to any contaminating substance and temperature change. **Figure 1a** provides detailed illustrations of the fabrication procedure for obtaining a residue-free region. We successfully attain residue-free MoS_2 through the following steps: i) pre-exfoliation of bulk crystal MoS_2 with the slide glass/double-sided tape for 3–4 times repeatedly, not only to expose the intrinsic and flat region but also to achieve thin and large-area flakes, ii) gentle attachment of the tape stamp to the pre-exfoliated material at an angle of ≈5° to ensure stable contact, and iii) exfoliation of the residue-free region along with the tape stamp. A large-area pristine flake is achievable due to the nature of 2D materials; weaker interlayer vdW force compared to in-plane covalent bonding. Subsequently, a part of the residue-free region is transferred onto the substrate (300 nm-thick SiO_2/Si), maintaining the angle of the tape stamp in order to prevent it from contaminating the substrate.

Because some transferred residue-free parts may not be of sufficient quality in terms of uniformity, flatness, etc., it is necessary to transfer only the intact region selectively via SM or TM. Figure 1b,c depict illustrations of SM and TM, respectively, along with corresponding AFM topographies that confirm the high quality of the transferred flakes. The transfer of a target flake onto a substrate is made based on the adhesion energy between the residue-free region and the substrate, which either exceeds the interlayer vdW energy for SM or holds the material to tear off the undesirable region for TM. After the target flake is transferred, the remaining residue-free region, referred to as the RFS, can be employed diversely to manipulate flakes, as detailed in Section 2.4. The details about the fabrication procedures are provided in Figure S1 and Videos S1–S3 (Supporting Information). The adoption of an RFS prevents possible contaminations from the tape stamp and also minimizes the risk of mechanical damage to the target flake by relying solely on vdW forces. The process is performed under ambient conditions and is completed within a few minutes due to its simplicity, as it employs the tape stamp without additional tools. Representative AFM topography images of flakes obtained via SM and TM show an absence of impurities and exhibit remarkable flatness, with root-mean-square roughness (R_q) of ≈0.061 and ≈0.187 nm, respectively, compared to that of fresh cleavage MoS_2 (R_q ≈0.23 ± 0.03 nm, thickness 8–17 nm).[2]

Additional flakes with diverse geometries were fabricated to explore the feasibility of SM and TM, and their corresponding flake qualities. Figure 1d represents the thickness and R_q results of the flakes transferred by SM and TM, indicating the potential of our technique for producing high-quality and ultra-thin flakes. Although precise thickness and shape control with the mechanical exfoliation method is difficult, there exists a certain accessible thickness range for each of the two transfer methods.[21,22] SM

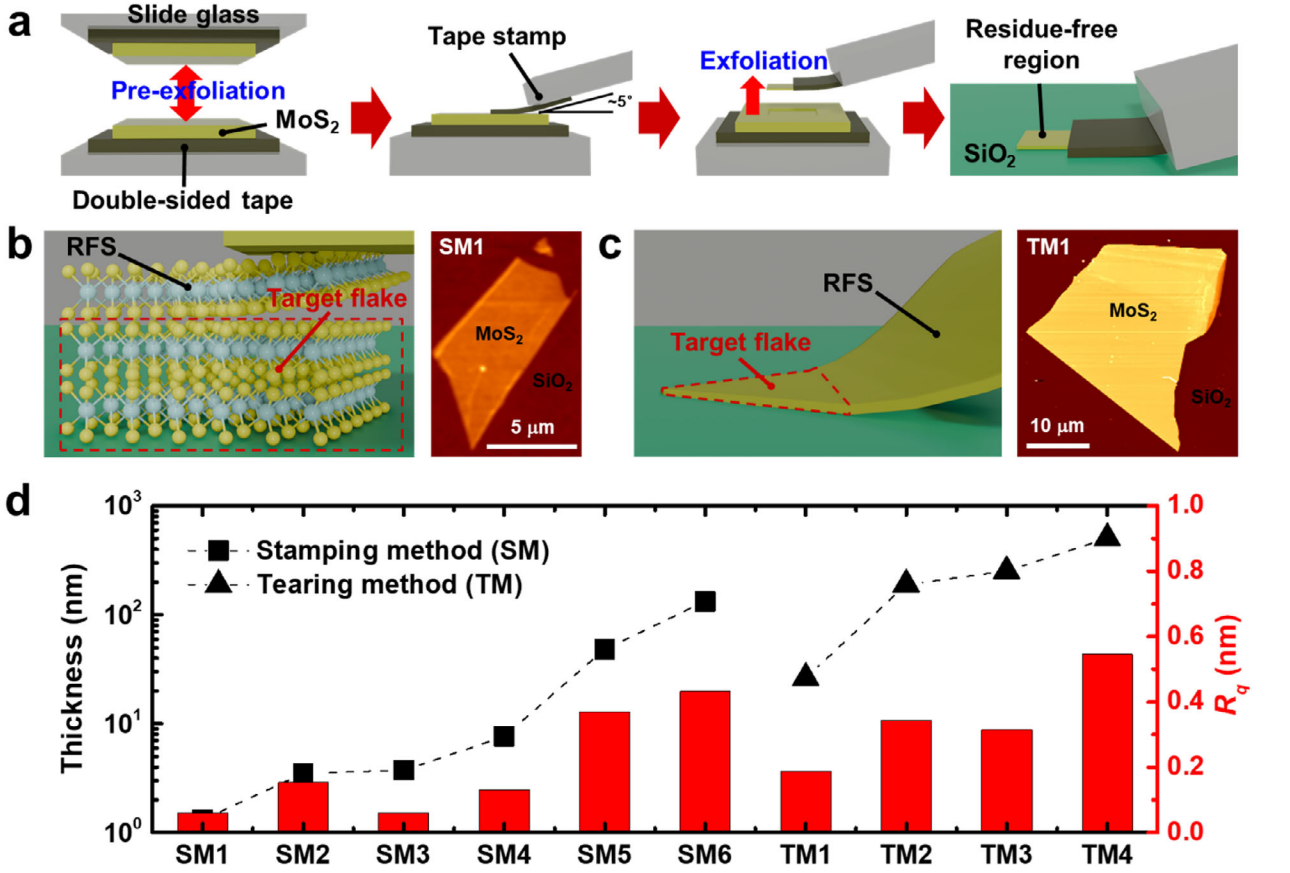

Figure 1. The fabrication procedure for residue-free MoS_2 flakes. a) Schematic illustrations of the achievement of a residue-free region using the tape stamp. b) The SM and c) TM approaches for transferring the target flake onto a SiO_2 substrate, along with AFM topography images of the transferred target flake (SM1 and TM1). These approaches enable the simultaneous achievement of both the residue-free stamp (RFS) and target flake. d) The results of accessible thickness and R_q for SM and TM.

produces thinner flakes, of which the thicknesses range from bilayer to a hundred nanometers, via delamination between layers of the residue-free region, while TM produces relatively thicker flakes via tearing off part of the residue-free region. The ability to produce residue-free 2D materials across a wide thickness range not only supports advancement in nanoelectronic devices but also provides an excellent substrate for epitaxial growth and thermal management.[23–27] The thickness, area, and R_q values of SM1–6 and TM1–4 flakes are presented in Figures S2, S3 and Tables S1 and S2 (Supporting Information). For thinner flakes, a few bright spots on the surface are observed, as shown in Figure S2 (Supporting Information). These spots are attributed to either MoS_2 debris or the presence of blisters, as evidenced by backscattered electron images (Figure S4, Supporting Information). Consequently, we selectively employed SM and TM depending on the required thickness of the target residue-free flakes, which can also be performed multiple times within a single residue-free region to achieve the desired flakes. Despite an increase in roughness with thickness, the values still remained below ≈0.6 nm, which are fairly excellent result considering that previous work reported an R_q of ≈0.7 nm for a thickness of 63 nm.[28]

2.2. Characterizations of the residue-free MoS_2

The quality of the transferred residue-free 2H-MoS_2 was investigated using an HR-TEM equipped with energy dispersive spectroscopy (EDS) for direct visualization of atomic structures and compositions. **Figure** 2a,b show TEM images of the flake, transferred onto a nickel grid using SM, demonstrating the successful creation of a suitably thin-layered flake for detailed examination of its atomic arrangement. Corresponding selected area electron diffraction (SAED) patterns exhibit a hexagonal symmetrical diffraction pattern of spots, i.e., a characteristic of the defect-free and high-crystalline 2H phase of MoS_2.[29,30] Additionally, the HR-TEM image obviously confirms a hexagonal structure of the flake as shown in Figure 2c. The inset presents that the intensity profile obtained along the red arrow provides the distributions of Mo and S atoms. The lattice constant is extracted as 3.13 ± 0.1 Å for the nearest Mo—Mo distance. The relatively lower intensity of S atoms, consistent with pristine 2H-MoS_2 structures, is attributed to the different positions of Mo and S atoms along the c-axis.[30] Furthermore, Mo and S atoms are uniformly distributed throughout the flake (Figure 2d,e), indicative of material homogeneity, and as expected, C and O atoms, involving

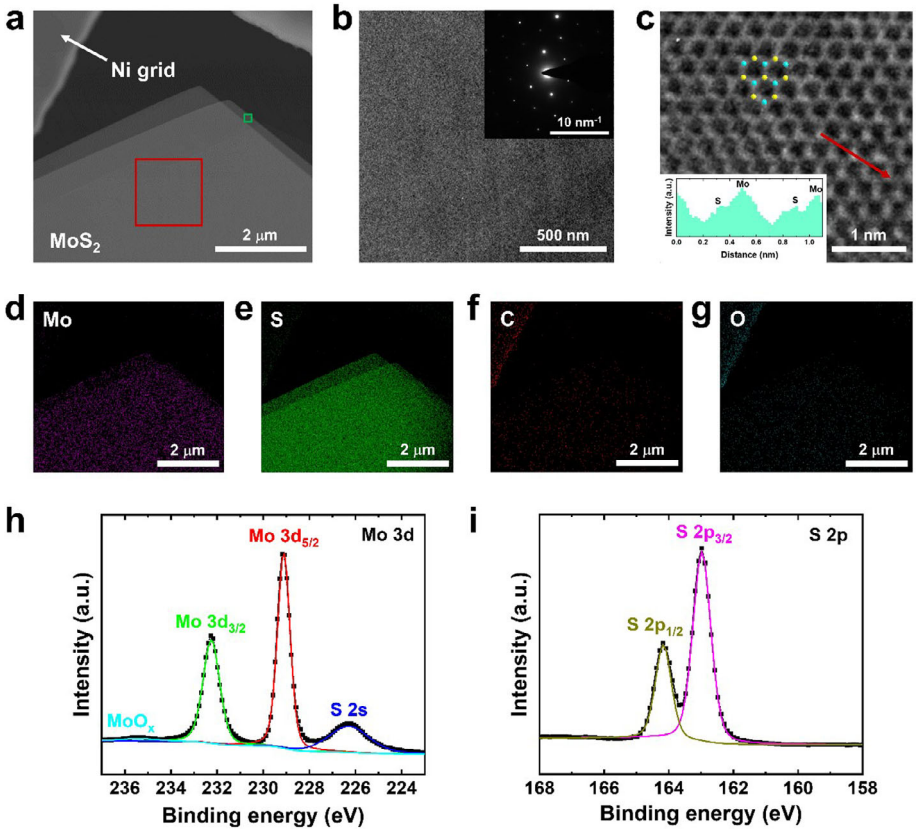

Figure 2. Characterizations of the residue-free MoS_2 flakes. TEM images of a) the flake transferred onto a nickel grid and b) a zoomed-in view of the area indicated by the red box in (a). Inset: corresponding SAED pattern. c) HR-TEM image (the green box in (a)), highlighting Mo atoms (cyan dots) and S atoms (yellow dots) arranged on a hexagonal lattice for the 2H phase. Inset: intensity profile along the red arrow, indicating Mo and S atoms. d–g) EDS elemental mappings for Mo, S, C, and O atoms, respectively. Representative XPS spectra (TM3) illustrating the h) Mo 3d and i) S 2p peaks.

polymeric residue or oxidation on the surface, are barely observed, respectively (Figure 2f,g).

For further analysis of the chemical compositions within the 2H-MoS_2 flake, XPS was employed. In Figure 2h, the Mo 3d spectrum shows distinct peaks corresponding to Mo $3d_{5/2}$ (≈229 eV), Mo $3d_{3/2}$ (≈232 eV), and S 2s (≈226.3 eV). Additionally, Figure 2i shows well-defined peaks for S $2p_{3/2}$ and S $2p_{1/2}$ at ≈161.9 and 163 eV, respectively. The negligible peak at ≈236 eV, associated with the oxidation of Mo (MoO_x), is consistent with the EDS mapping results. Moreover, all the peak binding energies (BE) from these XPS characterizations closely match those reported in the previous studies.[31,32] When comparing with the pre-exfoliated MoS_2 (Pre1) and an unprocessed bulk crystal for further validation, the peak BEs and small intensity of MoO_x peaks of TM2–4 exhibit excellent agreements with each other, as illustrated in Figure S5 and Table S3 (Supporting Information). This consistency underscores the reliability and reproducibility of our residue-free fabrication technique, which minimizes the generation of mechanical defects, residues, and oxidation.

2.3. Electrical Performance and Strain Analysis

The characterization of the carrier mobility, on/off ratio, and applied strain of residue-free MoS_2 was conducted on different scales with four FETs (S_{FET} 1–4 as shown in Figure S6, Supporting Information) and employing Raman spectroscopy. **Figure 3**a illustrates a schematic of a back-gated MoS_2 FET, accompanied by a representative optical image of the measured device (S_{FET} 4). The devices comprised transferred MoS_2 flakes on metal electrodes (5 nm-thick Cr/40 nm-thick Au) and gate dielectric layers (300 nm-thick thermally grown SiO_2). To prevent exposure to polymer resists during photo- and electron-beam lithography, the flakes were transferred after fabricating the metal electrodes (Video S4, Supporting Information). To achieve stable contact between the flake and the metal electrodes, two approaches were employed: the elimination of burrs on the edges of metal electrodes (Figure S7a, Supporting Information), and a vacuum annealing process.[33] After a sufficient annealing duration of over 16 h, the contact behavior shifted from Schottky to ohmic, resulting in a significant improvement in the source-drain current (I_{SD}) and a marked reduction in contact resistance (Figure S7b, Supporting Information). This vacuum annealing process effectively reduces hysteresis and enhances electrical performance by desorbing the gas molecules from the MoS_2 channel. Additionally, it promotes doping, which is attributed to the presence of vacancies or the reduction of polymer contamination.[2,34,35] However, the minimal variation in threshold voltage between 4 and 16 h of annealing suggests that the transferred MoS_2 remains free from mechanical damage and polymer residue. Furthermore,

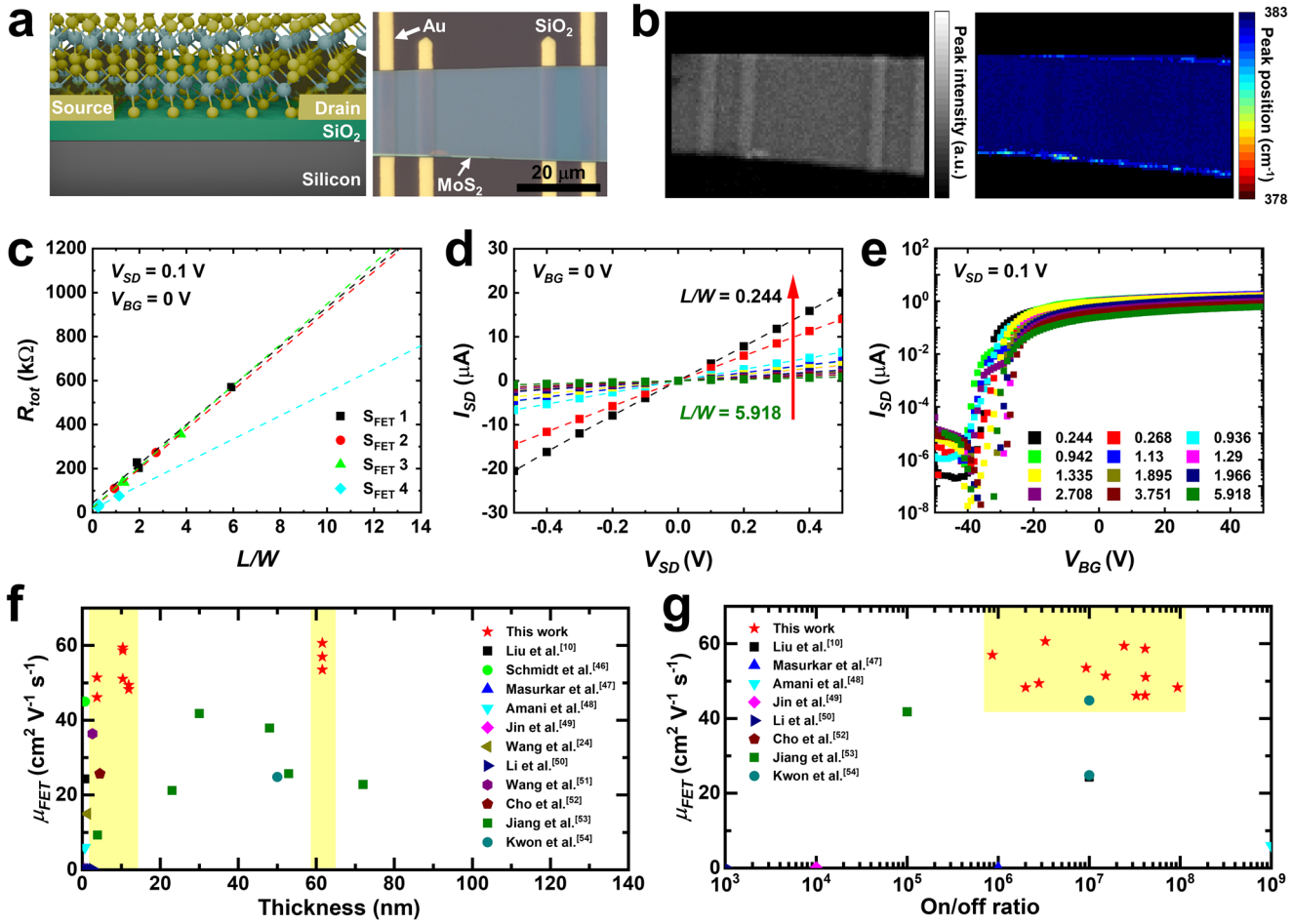

Figure 3. Electrical and strain characterizations of residue-free MoS_2. a) Schematic and representative optical image of the back-gated MoS_2 FET (S_{FET} 4). b) Raman spectroscopy map illustrating the peak intensity and position of E^1_{2g} mode. c) Total resistance versus L/W to extract the contact resistance. d) Output curve and e) transfer curve for different L/W ratios. Benchmark plots of μ_{FET} as a function of f) thickness and g) on/off ratio of MoS_2 FET with a SiO_2 gate dielectric and Au contact.

because the field-effect mobility (μ_{FET}) of MoS_2 FET devices is influenced by applied strain, it is necessary to investigate whether our method imposed strain on the MoS_2 flakes, considering that they were fabricated without any support layer such as PMMA or adhesive tape.[36,37] Figure 3b shows the Raman mapping for peak intensity and position of E^1_{2g} mode for S_{FET} 4, which exhibits a greater sensitivity to the shift induced by strain.[38,39] Despite including MoS_2 on the metal electrodes in the Raman mapping, which is indicated by the relatively large intensity, the strain across the entire region was negligible, as evidenced by the E^1_{2g} peak at ≈383 cm^{-1}.[40,41] Therefore, the following results can be considered as the strain-free properties of MoS_2.

The electrical performance of the MoS_2 FETs was measured using a vacuum probe station. Figure 3c shows the total resistance (R_{tot}) plotted with respect to the ratio of length (L) to width (W) at a back-gate voltage of 0 V (V_{BG}) to extract the contact resistance (R_C). Based on the 2D transfer length method (2D TLM), the R_C values are determined from the intercept of the y-axis of a linear fit. The contact resistivity ($R_{SC} = W \times R_C$) ranged from 45.70 to 160.4 kΩ μm. Although a proper vacuum annealing process and well-structured metal electrodes were employed, significantly higher R_{SC} values and their wider range were observed compared to those between Au electrodes and monolayer (≈42 kΩ μm) and few-layer MoS_2 (≈18 kΩ μm).[23,42] This discrepancy is likely due to the rough surfaces of the sputtered Au electrodes and the formation of gas-filled nanoblisters at the interface during the transfer onto the electrodes.[43–45] Nevertheless, Figure 3d,e demonstrate the linearity of the output curves and on/off ratios of 10^6–10^8. Owing to the absence of the residue, the extracted μ_{FET} and an on/off ratio outperform those of the previous works, which were obtained from MoS_2 FET with SiO_2 gate dielectric and Au electrode, as shown in the benchmark plots (Figure 3f,g).[10,24,46–54] A detailed summary of the data presented in the benchmark plot is provided in Table S4 (Supporting Information). The values of μ_{FET} range from 46.11 to 60.66 cm^2 V^{-1} s^{-1} with high on/off ratio values.

2.4. Manipulation Techniques and Heterostructure Assembly

Having discussed the fabrication and characterization processes above, we will now explain the various manipulation methods.

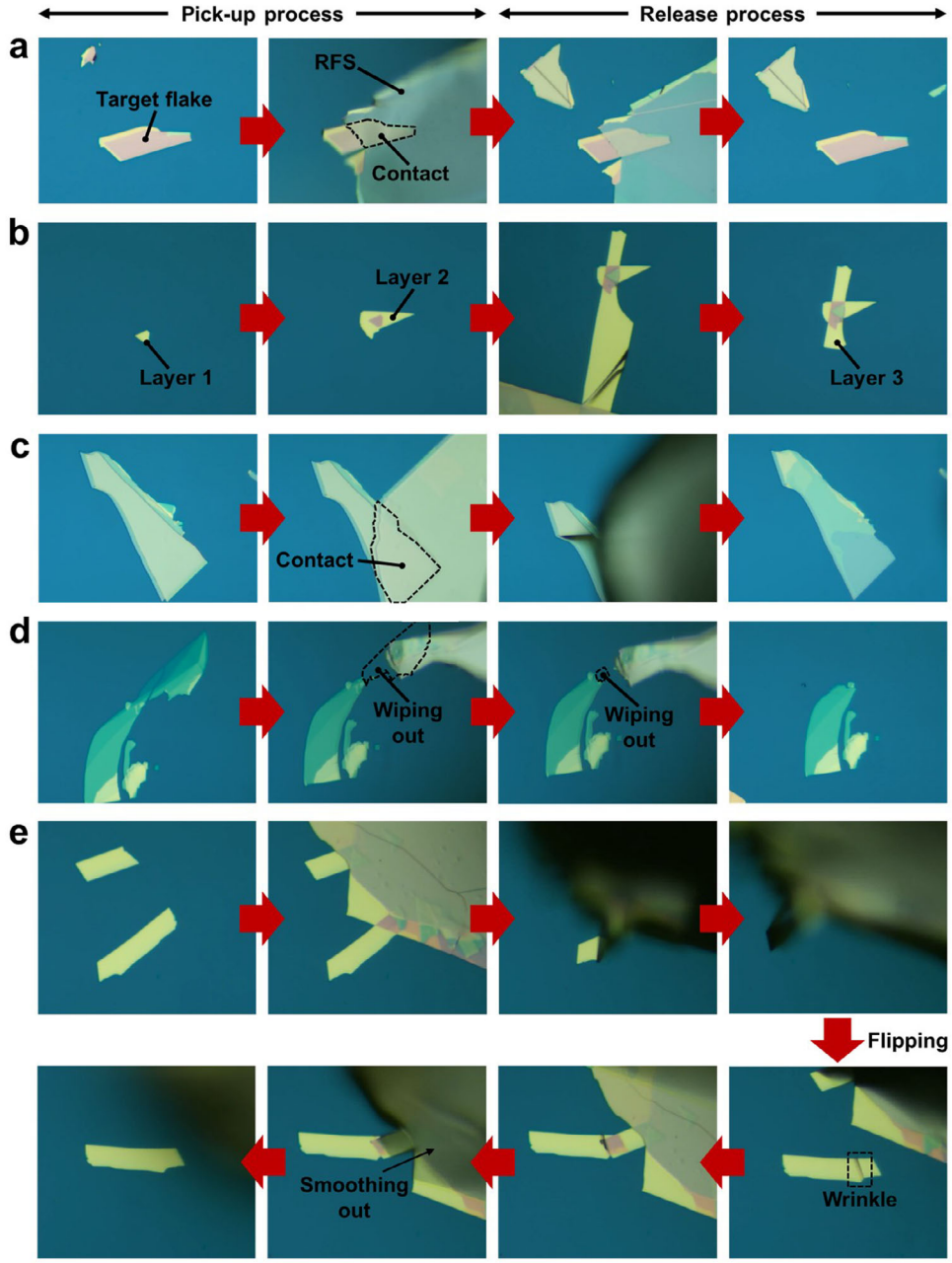

Figure 4. Manipulation techniques of MoS_2 flake with RFS. Optical images of the procedures for a) pick-up and release, b) stacking, c) exfoliation, d) wiping-out, e) flipping, and smoothing-out processes.

The versatility of our manipulation techniques with the RFS is demonstrated in **Figure 4** (see Videos S5–S10, Supporting Information for details). In the pick-up and release processes (Figure 4a), the RFS starts making a sufficiently large contact with the target flake, thereby the adhesion between them surpasses that between the target flake and the substrate. The pick-up process was conducted with vertical movement of the RFS and it is facilitated by the higher interlayer adhesion energy of MoS_2/MoS_2 ($\approx$0.384 J m^{-2}) compared to that of MoS_2/SiO_2 ($\approx$0.189 J m^{-2}) and the flexibility of RFS allowing for a stable adhesion to the target flake until the flake is completely picked up from the substrate (Figure S8a, Supporting Information).[20] The RFS, carrying the picked-up flake, then carefully moves and subsequently releases it onto another position on the substrate. During the release process, an almost the entire portion of the flake is first in touch with the substrate, and then the RFS slides without an imposed pressure in a way that reduces the overlap area between the RFS and the target flake, which leaves the target flake behind (Figure S8b, Supporting Information). For further application of the pick-up and release, the RFS facilitates layer staking with precise positioning (Figure 4b), as demonstrated in the optical images, which show triple-stacked distinct layers and a clear

overlap area. The techniques also enable tailoring the target flake through exfoliation and wiping-out processes, thereby improving the yield of the target flakes. The exfoliation process could occur when there exists an interface with comparatively weak adhesion in the target flake, distinguishing itself from the pick-up process (Figure 4c). Such an interface with weak adhesion serves as an initial separation point, allowing for exfoliation at a large peeling angle and decreasing the required peeling force for exfoliation.[55] Even if the yield is low, it is expected that peeling or leaving a thin layer will be possible as long as an initial separation point exists. The wiping-out technique implements precise and repeatable removal of unwanted thin regions (Figure 4d). Furthermore, the RFS can reliably flip and smooth out a target flake. Specifically, in the smoothing-out process, the RFS gently pulls the target flake to unfold the wrinkle on the flake (Figure 4e). Additionally, the RFS can be used to intentionally create wrinkles in the flake, which results in the presence of strain, and after smoothing, the absence of strain is confirmed, as provided in Figure S10 and Video S11 (Supporting Information). Utilizing the RFS provides a comprehensive set of manipulations, including pick-up and release, stacking, exfoliation, wiping-out, as well as flipping and smoothing-out processes, which are substantially useful for fabricating complex and high-quality 2D material-based devices.

To evaluate the feasibility of complex manipulation techniques using the same material-based RFS, we explored the mechanisms behind the pick-up and release processes through a combination of experiments and analytical calculations. Unlike the relatively straightforward behavior of robust adhesive polymers, manipulation based on 2D materials and vdW interactions involves more intricate dynamics, such as stick-slip behavior and ultralow frictional sliding (commonly referred to as superlubricity).[56,57] The success of the pick-up process relies on the initial peeling stiffness at the flake/RFS interface (MoS_2/MoS_2) surpassing that at the flake/substrate interface (MoS_2/SiO_2). The stiffness is influenced by both adhesion energy and the relative thickness of the target flake and RFS, which impact elastic strain energy and bending modulus.[58] In our case, the elastic strain energy can be considered negligible, as the in-plane stiffness of MoS_2 is significantly larger than the adhesion energy by a factor of three.[59,60] However, the bending modulus (D), which scales with thickness ($D \approx t^3$), becomes critical.[61] Figure S8c (Supporting Information) presents the optical image of flakes with varying thicknesses (M1–M5) and the applied RFS during the pick-up and release processes, with the corresponding thicknesses summarized in Table S5 (Supporting Information). Despite the high vdW adhesion energy of the flake/RFS interface, the experiments demonstrated that thinner flakes (M1 and M2) were successfully picked up, whereas thicker flakes (M3–M5) were not, emphasizing the role of relative thickness in determining manipulation success (see Video S12, Supporting Information). The pick-up process can be described as a 90-degree peeling event, considering the vertical movement and flexibility of RFS. The initial peeling stiffness ratio ($K_{pick\text{-}up}$), i.e., the ratio of the stiffness of flakes with RFS to those with the substrate, implies that a thicker RFS is more conducive to a stable pick-up process, as shown in Figure S8d (Supporting Information). Notably, flake M3, with a stiffness ratio of ≈1, was not picked up, likely attributed to repeated use of the RFS and airborne contaminants reducing the adhesive energy.[20,62] In contrast, the release process is better explained as frictional sliding between the 2D materials, influenced by the shear direction movement of the RFS. The shear strength value of the MoS_2/SiO_2 interface is greater than that of the MoS_2/MoS_2 interface, resulting from the superlubricity that arises from the incommensurate domains at the interfaces between 2D materials.[63–66] Figure S8e (Supporting Information) shows the initial sliding stiffness ratio ($K_{release}$), confirming that all flakes can be released. Additionally, the release process was successful when the entire surface of the target flake was covered with the same material-based RFS, demonstrating that the release process is independent of the overlap area between the target flake and RFS, consistent with previous studies (see Videos S13 and S14, Supporting Information for MoS_2 and h-BN, respectively).[58] However, applying force only in the shear direction is essential for an effective release process, as it maintains a minimal peeling angle between the target flake and the RFS. When the force was applied to the RFS without a sufficient distance from the target flake, the release process failed even though the entire surface of the target flake was not yet covered, as shown in Figure S9 (the details in Video S15, Supporting Information). This failure resulted from an increased peeling angle, which intensified the contribution of adhesion in the normal direction, potentially leading to the pick-up process instead of release. These experimental results confirm that the pick-up and release processes originate from the peeling and sliding mechanisms, respectively.

Figure 5a shows optical images of the assembly procedure for an h-BN/MoS_2/MLG vdW heterostructure. Using the same material-based RFS, each layer was precisely stacked in its designated locations to complete the structure. Moreover, we demonstrated that the pick-up and release process can be performed with diverse material combinations of target flakes and RFSs, of which the materials are allowed to be either identical to or different from each other (see Videos S16–S24, Supporting Information for details). These trials aim to show the expandability of our techniques to other materials. Specifically, MLG and h-BN were chosen due to their frequent use as electrodes and dielectric layers, respectively, in 2D material-based devices. While examining the vdW heterostructure assemblies using AFM, we found no significant surface contamination or mechanical defect, such as wrinkles and blisters, in the individual layers, comprising the heterostructure (Figure 5b). However, a notable concentration of blisters was observed specifically at the heterostructure interface. Therefore, the observed blisters were successfully removed using an AFM-tip squeezing technique, which enables the effective elimination of blisters.[67–69] To prevent mechanical damage to the heterostructure, the applied force was gradually increased from 5 to 2000 nN during the process (Figure S11, Supporting Information). Following the squeezing process, the thickness profile accurately reflected the individual layer thicknesses, as well as the R_q value exhibited a significant improvement from 0.707–1.477 nm to 0.097–0.208 nm (Figure S12, Supporting Information). Separately, we demonstrated the capability to fabricate MoS_2/h-BN/MLG with alternative stacking order, which could be applied to vdW heterostructures (Figure S13, Supporting Information).[70] Additionally, sufficiently thin h-BN layers (≈3.54 nm) can be fabricated using our method (Figure S14, Supporting Information). The high quality of the vdW heterostructure was achieved by benefitting from the versatility of

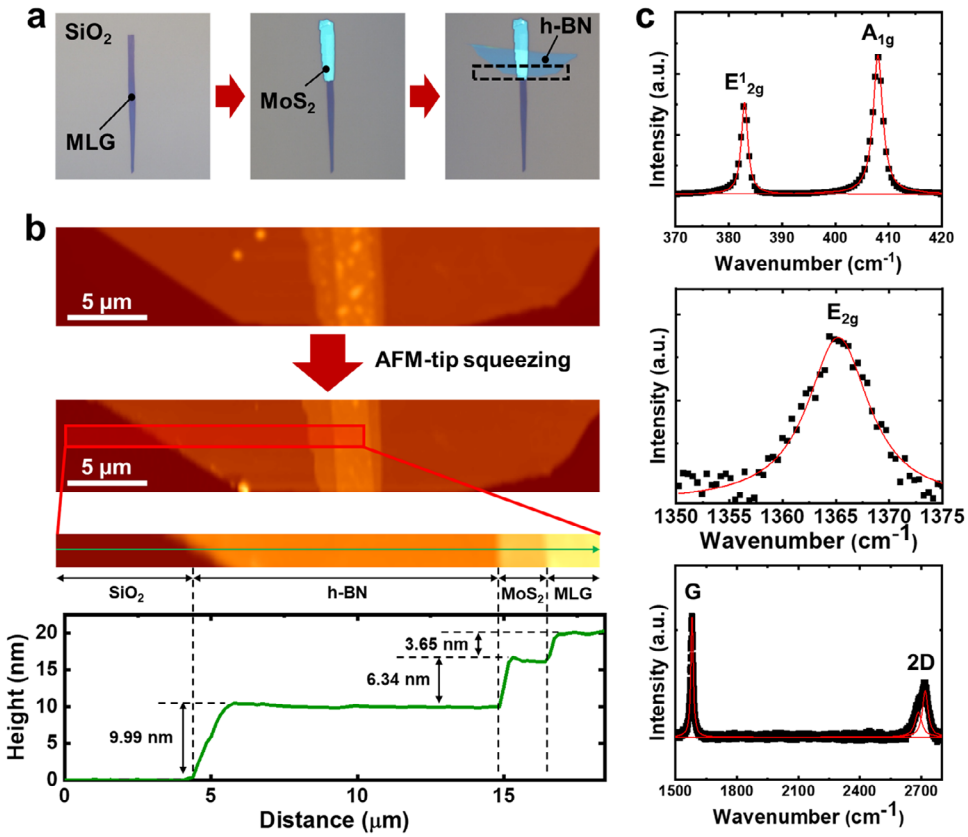

Figure 5. h-BN/MoS_2/MLG vdW heterostructure. a) Fabrication procedure of the heterostructure. b) AFM topography images before and after the AFM-tip squeezing process. An enlarged image (red box) depicting heterostructure assembly and height profiles along the green arrow. The thicknesses of h-BN, MoS_2, and MLG are 9.99, 6.34, and 3.65 nm, respectively. c) Representative Raman spectra measured at h-BN/MoS_2/MLG assembly after the squeezing process, with Lorentzian fitting shown in red lines. The intensities are magnified to account for relatively low intensity.

our manipulation techniques, including smoothing out wrinkles, removal of undesired areas, and ensuring precise re-positioning.

Furthermore, Raman analysis was conducted to characterize the heterostructure assembly following the AFM-tip squeezing process (Figure 5c). The Raman peak positions of the h-BN/MoS_2/MLG are ≈1580 and ≈2719 cm^{-1}, corresponding to the G and 2D modes of MLG, respectively.[71] Additionally, the $E_{2\,g}$ mode of h-BN appears at ≈1365 cm^{-1}, and the $E^1_{2\,g}$ and $A_{1\,g}$ modes of MoS_2 are observed at ≈383 and ≈408 cm^{-1}.[40,41,72,73] However, no distinct peak shifts were observed in the not-squeezed region, specifically with the $E^1_{2\,g}$ mode shifting by up to 0.11 cm^{-1} and the $E_{2\,g}$ mode shifting by 0.29 cm^{-1} (Figure S12, Supporting Information). This is likely due to insufficient measurement area in the not-squeezed region. In contrast, the MoS_2/h-BN/MLG heterostructure exhibited redshifts of 0.3, 1.1, and 0.86 cm^{-1} in the $E_{2\,g}$, $E^1_{2\,g}$, and $A_{1\,g}$ modes, respectively (Figure S13, Supporting Information). Considering the slight redshift observed in $E_{2\,g}$ mode of h-BN and $E^1_{2\,g}$ mode of MoS_2, these changes indicate the presence of strain rather than a doping effect.[38,39,74] These redshifts were observed only in the transferred upper layers of the heterostructure (MoS_2 and h-BN), and are attributed to the strain induced by blisters. However, phenomena such as peak splitting due to symmetry breaking were not observed here, suggesting that no severe strain was imposed on the heterostructure.[36,75] Consequently, the AFM-tip squeezing process and Raman spectroscopy demonstrate the excellent flatness of the vdW heterostructure interfaces, without applied strain, verifying the effectiveness and versatility of our manipulation techniques.

3. Conclusion

In summary, a residue-free fabrication method for 2D materials was developed utilizing vdW interactions, without exposure to additional substances or temperature changes. Leveraging the high interfacial adhesion energy of MoS_2, we conducted fabrications of MoS_2 flakes with diverse thicknesses ranging from bilayer to several hundreds of nanometers. Notably, it was confirmed that SM and TM can be selectively applied based on the required thickness, as their principles involve interlayer delamination and tearing of the residue-free region, respectively. Comprehensive investigations of morphologies, chemical compositions, and strain reveal the high quality of the residue-free flakes obtained by our method, exhibiting remarkable flatness, absence of contaminations, mechanical damage, and pre-strain. Furthermore, an excellent FET mobility of up to 60 $cm^2\ V^{-1}\ s^{-1}$ and an on/off ratio of ≈10^8 were achieved from the MoS_2 FET devices fabricated using our fabrication techniques. Additionally, the RFS enables diverse manipulation techniques such as pick up and release, exfoliation, stacking, wiping out, flipping, and

smoothing out. These techniques were successfully used to assemble the vdW heterostructure, demonstrating the adaptability of this method to diverse materials. We anticipate that the proposed method can be readily applied to the fabrication of high-quality 2D material-based devices, thereby significantly expanding the application potential of 2D materials in various fields.

Supporting Information

Supporting Information is available from the Wiley Online Library or from the author.

Acknowledgements

M.L. and C.K. contributed equally to this work. This research was supported by the National Research Foundation (NRF) of Korea grant funded by the Korea government (the Ministry of Science and ICT) (2022R1A2C2007587, RS-2023-00218908, and RS-2024-00408180) and GIST-MIT Research Collaboration grant funded by the GIST.

Conflict of Interest

The authors declare no conflict of interest.

Data Availability Statement

The data that support the findings of this study are available from the corresponding author upon reasonable request.

Keywords

heterostructure, manipulation, residue-free fabrication, 2D materials, van der Waals interactions

Received: November 29, 2024
Revised: February 18, 2025
Published online:

[1] W. Choi, M. A. Shehzad, S. Park, Y. Seo, *RSC Adv.* **2017**, *7*, 6943.
[2] J. Liang, K. Xu, B. Toncini, B. Bersch, B. Jariwala, Y. Lin, J. Robinson, S. K. Fullerton-Shirey, *Adv. Mater. Interfaces* **2019**, *6*, 1801321.
[3] Y.-C. Lin, C. Jin, J.-C. Lee, S.-F. Jen, K. Suenaga, P.-W. Chiu, *ACS Nano* **2011**, *5*, 2362.
[4] M. T. Pettes, I. Jo, Z. Yao, L. Shi, *Nano Lett.* **2011**, *11*, 1195.
[5] A. Pirkle, J. Chan, A. Venugopal, D. Hinojos, C. W. Magnuson, S. McDonnell, L. Colombo, E. M. Vogel, R. S. Ruoff, R. M. Wallace, *Appl. Phys. Lett.* **2011**, *99*, 122108.
[6] S. R. Cho, S. Ahn, S. H. Lee, H. Ha, T. S. Kim, M. Jo, C. Song, T. H. Im, P. Rani, M. Gyeon, K. Cho, S. Song, M. S. Jang, Y.-H. Cho, K. J. Lee, K. Kang, *Adv. Funct. Mater.* **2021**, *31*, 2105302.
[7] G. Woo, H.-U. Kim, H. Yoo, T. Kim, *Nanotechnology* **2021**, *32*, 045702.
[8] A. Mondal, C. Biswas, S. Park, W. Cha, S.-H. Kang, M. Yoon, S. H. Choi, K. K. Kim, Y. H. Lee, *Nat. Nanotechnol.* **2024**, *19*, 34.
[9] M. Velický, G. E. Donnelly, W. R. Hendren, S. McFarland, D. Scullion, W. J. I. DeBenedetti, G. C. Correa, Y. Han, A. J. Wain, M. A. Hines, D. A. Muller, K. S. Novoselov, H. D. Abruña, R. M. Bowman, E. J. G. Santos, F. Huang, *ACS Nano* **2018**, *12*, 10463.
[10] H. Liu, Q. H. Thi, P. Man, X. Chen, T. Chen, L. W. Wong, S. Jiang, L. Huang, T. Yang, K. H. Leung, T. T. Leung, S. Gao, H. Chen, C.-S. Lee, M. Kan, J. Zhao, Q. Deng, T. H. Ly, *Adv. Mater.* **2023**, *35*, 2210503.
[11] L. Wang, I. Meric, P. Y. Huang, Q. Gao, Y. Gao, H. Tran, T. Taniguchi, K. Watanabe, L. M. Campos, D. A. Muller, J. Guo, P. Kim, J. Hone, K. L. Shepard, C. R. Dean, *Science* **2013**, *342*, 614.
[12] J.-B. Lee, Y. R. Lim, A. K. Katiyar, W. Song, J. Lim, S. Bae, T.-W. Kim, S.-K. Lee, J.-H. Ahn, *Adv. Mater.* **2019**, *31*, 1904194.
[13] N. Huo, S. Tongay, W. Guo, R. Li, C. Fan, F. Lu, J. Yang, B. Li, Y. Li, Z. Wei, *Adv. Electron. Mater.* **2015**, *1*, 1400066.
[14] J. Chen, L. Liu, H. Chen, N. Xu, S. Deng, *ACS Appl. Mater. Interfaces* **2024**, *16*, 10877.
[15] Z. Dai, Y. Wang, L. Liu, J. Deng, W.-X. Tang, Q. Ou, Z. Wang, M. H. Uddin, G. Si, Q. Zhang, W. Duan, M. S. Fuhrer, C. Zheng, *Mater. Today Phys* **2022**, *27*, 100834.
[16] S. Masubuchi, M. Sakano, Y. Tanaka, Y. Wakafuji, T. Yamamoto, S. Okazaki, K. Watanabe, T. Taniguchi, J. Li, H. Ejima, T. Sasagawa, K. Ishizaka, T. Machida, *Sci. Rep.* **2022**, *12*, 10936.
[17] K. Jin, T. Wichmann, S. Wenzel, T. Samuely, O. Onufriienko, P. Szabó, K. Watanabe, T. Taniguchi, J. Yan, F. S. Tautz, F. Lüpke, M. Ternes, J. Martinez-Castro, *Adv. Mater. Interfaces* **2024**, *11*, 2300658.
[18] Y. Wakafuji, R. Moriya, S. Masubuchi, K. Watanabe, T. Taniguchi, T. Machida, *Nano Lett.* **2020**, *20*, 2486.
[19] W. Wang, N. Clark, M. Hamer, A. Carl, E. Tovari, S. Sullivan-Allsop, E. Tillotson, Y. Gao, H. de Latour, F. Selles, J. Howarth, E. G. Castanon, M. Zhou, H. Bai, X. Li, A. Weston, K. Watanabe, T. Taniguchi, C. Mattevi, T. H. Bointon, P. V. Wiper, A. J. Strudwick, L. A. Ponomarenko, A. V. Kretinin, S. J. Haigh, A. Summerfield, R. Gorbachev, *Nat. Electron.* **2023**, *6*, 981.
[20] H. Rokni, W. Lu, *Nat. Commun.* **2020**, *11*, 5607.
[21] N. Petrini, E. Peci, N. Curreli, E. Spotorno, N. Kazemi Tofighi, M. Magnozzi, F. Scotognella, F. Bisio, I. Kriegel, *Adv. Opt. Mater.* **2024**, *12*, 2303228.
[22] M. Yi, Z. Shen, *J. Mater. Chem. A* **2015**, *3*, 11700.
[23] H. Liu, A. T. Neal, P. D. Ye, *ACS Nano* **2012**, *6*, 8563.
[24] H. Wang, L. Yu, Y.-H. Lee, Y. Shi, A. Hsu, M. L. Chin, L.-J. Li, M. Dubey, J. Kong, T. Palacios, *Nano Lett.* **2012**, *12*, 4674.
[25] W. Yang, G. Chen, Z. Shi, C.-C. Liu, L. Zhang, G. Xie, M. Cheng, D. Wang, R. Yang, D. Shi, K. Watanabe, T. Taniguchi, Y. Yao, Y. Zhang, G. Zhang, *Nat. Mater.* **2013**, *12*, 792.
[26] A. Yan, J. J. Velasco, S. Kahn, K. Watanabe, T. Taniguchi, F. Wang, M. F. Crommie, A. Zettl, *Nano Lett.* **2015**, *15*, 6324.
[27] G. R. Jaffe, K. J. Smith, K. Watanabe, T. Taniguchi, M. G. Lagally, M. A. Eriksson, V. W. Brar, *ACS Appl. Mater. Interfaces* **2023**, *15*, 12545.
[28] S. Xiao, P. Xiao, X. Zhang, D. Yan, X. Gu, F. Qin, Z. Ni, Z. J. Han, K. (Ken) Ostrikov, *Sci. Rep.* **2016**, *6*, 19945.
[29] X. Wang, H. Feng, Y. Wu, L. Jiao, *J. Am. Chem. Soc.* **2013**, *135*, 5304.
[30] U. Maitra, U. Gupta, M. De, R. Datta, A. Govindaraj, C. N. R. Rao, *Angew. Chem., Int. Ed.* **2013**, *52*, 13057.
[31] G. Eda, H. Yamaguchi, D. Voiry, T. Fujita, M. Chen, M. Chhowalla, *Nano Lett.* **2012**, *12*, 526.
[32] L. P. L. Mawlong, A. Bora, P. K. Giri, *Sci. Rep.* **2019**, *9*, 19414.
[33] B. W. H. Baugher, H. O. H. Churchill, Y. Yang, P. Jarillo-Herrero, *Nano Lett.* **2013**, *13*, 4212.
[34] J.-H. Ahn, W. M. Parkin, C. H. Naylor, A. T. C. Johnson, M. Drndić, *Sci. Rep.* **2017**, *7*, 4075.
[35] Y. Park, N. Li, D. Jung, L. T. Singh, J. Baik, E. Lee, D. Oh, Y. D. Kim, J. Y. Lee, J. Woo, S. Park, H. Kim, G. Lee, G. Lee, C.-C. Hwang, *npj 2D Mater. Appl.* **2023**, *7*, 60.
[36] I. M. Datye, A. Daus, R. W. Grady, K. Brenner, S. Vaziri, E. Pop, *Nano Lett.* **2022**, *22*, 8052.
[37] Y. Liu, Y. Jiang, C. Tan, Y. Li, Y. Chen, Z. Li, L. Gao, L. Yang, Z. Wang, *Phys. status solidi – Rapid Res. Lett.* **2023**, *17*, 2300101.
[38] Y. Wang, C. Cong, C. Qiu, T. Yu, *Small* **2013**, *9*, 2857.

[39] M. Buscema, G. A. Steele, H. S. J. van der Zant, A. Castellanos-Gomez, *Nano Res.* **2014**, *7*, 561.
[40] G. L. Frey, R. Tenne, M. J. Matthews, M. S. Dresselhaus, G. Dresselhaus, *Phys. Rev. B* **1999**, *60*, 2883.
[41] H. Li, Q. Zhang, C. C. R. Yap, B. K. Tay, T. H. T. Edwin, A. Olivier, D. Baillargeat, *Adv. Funct. Mater.* **2012**, *22*, 1385.
[42] N. Kaushik, A. Nipane, F. Basheer, S. Dubey, S. Grover, M. M. Deshmukh, S. Lodha, *Appl. Phys. Lett.* **2014**, *105*, 113505.
[43] M. Velický, A. Rodriguez, M. Bouša, A. V. Krayev, M. Vondráček, J. Honolka, M. Ahmadi, G. E. Donnelly, F. Huang, H. D. Abrunã, K. S. Novoselov, O. Frank, *J. Phys. Chem. Lett.* **2020**, *11*, 6112.
[44] D. A. Sanchez, Z. Dai, P. Wang, A. Cantu-Chavez, C. J. Brennan, R. Huang, N. Lu, *Proc. Natl. Acad. Sci. USA* **2018**, *115*, 7884.
[45] F. Pizzocchero, L. Gammelgaard, B. S. Jessen, J. M. Caridad, L. Wang, J. Hone, P. Bøggild, T. J. Booth, *Nat. Commun.* **2016**, *7*, 11894.
[46] H. Kwon, W. Choi, D. Lee, Y. Lee, J. Kwon, B. Yoo, C. P. Grigoropoulos, S. Kim, *Nano Res.* **2014**, *7*, 1137.
[47] H. Schmidt, S. Wang, L. Chu, M. Toh, R. Kumar, W. Zhao, A. H. Castro Neto, J. Martin, S. Adam, B. Özyilmaz, G. Eda, *Nano Lett.* **2014**, *14*, 1909.
[48] N. Masurkar, N. K. Thangavel, S. Yurgelevic, S. Varma, G. W. Auner, L. M. Reddy Arava, *Biosens. Bioelectron.* **2021**, *172*, 112724.
[49] M. Amani, M. L. Chin, A. G. Birdwell, T. P. O'Regan, S. Najmaei, Z. Liu, P. M. Ajayan, J. Lou, M. Dubey, *Appl. Phys. Lett.* **2013**, *102*, 193107.
[50] T. Jin, J. Kang, E. Su Kim, S. Lee, C. Lee, *J. Appl. Phys.* **2013**, *114*, 164509.
[51] H. Li, Z. Yin, Q. He, H. Li, X. Huang, G. Lu, D. W. H. Fam, A. I. Y. Tok, Q. Zhang, H. Zhang, *Small* **2012**, *8*, 63.
[52] J. Wang, Q. Yao, C.-W. Huang, X. Zou, L. Liao, S. Chen, Z. Fan, K. Zhang, W. Wu, X. Xiao, C. Jiang, W.-W. Wu, *Adv. Mater.* **2016**, *28*, 8302.
[53] K. Cho, W. Park, J. Park, H. Jeong, J. Jang, T. Y. Kim, W. K. Hong, S. Hong, T. Lee, *ACS Nano* **2013**, *7*, 7751.
[54] J. Jiang, Y. Zhang, A. Wang, J. Duan, H. Ji, J. Pang, Y. Sang, X. Feng, H. Liu, L. Han, *ACS Appl. Electron. Mater.* **2020**, *2*, 2132.
[55] Z. Wei, K. Lin, X. Wang, Y.-P. Zhao, *Compos. Part A Appl. Sci. Manuf.* **2021**, *150*, 106592.
[56] G. Ru, W. Qi, K. Tang, Y. Wei, T. Xue, *Tribol. Int.* **2020**, *151*, 106483.
[57] C. Lee, Q. Li, W. Kalb, X.-Z. Liu, H. Berger, R. W. Carpick, J. Hone, *Science.* **2010**, *328*, 76.
[58] Z. Xue, G. Chen, C. Wang, R. Huang, *J. Mech. Phys. Solids* **2022**, *158*, 104698.
[59] S. Bertolazzi, J. Brivio, A. Kis, *ACS Nano* **2011**, *5*, 9703.
[60] G. Ulian, G. Valdrè, *J. Appl. Crystallogr.* **2023**, *56*, 611.
[61] G. Casillas, U. Santiago, H. Barrón, D. Alducin, A. Ponce, M. José-Yacamán, *J. Phys. Chem. C* **2015**, *119*, 710.
[62] S. R. Na, Y. Kim, C. Lee, K. M. Liechti, J. W. Suk, *Sci. Rep.* **2017**, *7*, 14740.
[63] Y. Liu, A. Song, Z. Xu, R. Zong, J. Zhang, W. Yang, R. Wang, Y. Hu, J. Luo, T. Ma, *ACS Nano* **2018**, *12*, 7638.
[64] M. Liao, P. Nicolini, L. Du, J. Yuan, S. Wang, H. Yu, J. Tang, P. Cheng, K. Watanabe, T. Taniguchi, L. Gu, V. E. P. Claerbout, A. Silva, D. Kramer, T. Polcar, R. Yang, D. Shi, G. Zhang, *Nat. Mater.* **2022**, *21*, 47.
[65] Y. Sun, Y. Wang, E. Wang, B. Wang, H. Zhao, Y. Zeng, Q. Zhang, Y. Wu, L. Gu, X. Li, K. Liu, *Nat. Commun.* **2022**, *13*, 3898.
[66] G. Wang, Z. Dai, Y. Wang, P. Tan, L. Liu, Z. Xu, Y. Wei, R. Huang, Z. Zhang, *Phys. Rev. Lett.* **2017**, *119*, 36101.
[67] M. R. Rosenberger, H.-J. Chuang, K. M. McCreary, A. T. Hanbicki, S. V. Sivaram, B. T. Jonker, *ACS Appl. Mater. Interfaces* **2018**, *10*, 10379.
[68] Y. Kim, P. Herlinger, T. Taniguchi, K. Watanabe, J. H. Smet, *ACS Nano* **2019**, *13*, 14182.
[69] M. R. Rosenberger, H.-J. Chuang, M. Phillips, V. P. Oleshko, K. M. McCreary, S. V. Sivaram, C. S. Hellberg, B. T. Jonker, *ACS Nano* **2020**, *14*, 4550.
[70] O. H. Gwon, J. Y. Kim, H. S. Kim, S. J. Kang, H. R. Byun, M. Park, D. S. Lee, Y. jeong Kim, S. Ahn, J. Kim, S. J. Cho, Y. J. Yu, *Adv. Funct. Mater.* **2021**, *31*, 2105472.
[71] H. Hiura, T. W. Ebbesen, K. Tanigaki, H. Takahashi, *Chem. Phys. Lett.* **1993**, *202*, 509.
[72] S. Reich, A. C. Ferrari, R. Arenal, A. Loiseau, I. Bello, J. Robertson, *Phys. Rev. B* **2005**, *71*, 205201.
[73] M. Koperski, D. Vaclavkova, K. Watanabe, T. Taniguchi, K. S. Novoselov, M. Potemski, *Proc. Natl. Acad. Sci* **2020**, *117*, 13214.
[74] E. Blundo, A. Surrente, D. Spirito, G. Pettinari, T. Yildirim, C. A. Chavarin, L. Baldassarre, M. Felici, A. Polimeni, *Nano Lett.* **2022**, *22*, 1525.
[75] S. Parmar, A. Biswas, S. K. Singh, B. Ray, S. Parmar, S. Gosavi, V. Sathe, R. Janay Choudhary, S. Datar, S. Ogale, *Phys. Rev. Mater.* **2019**, *3*, 74007.